Multi-color laser excitation of diamond nitrogen vacancy centers embedded in nanophotonic structures

🆔 Axel Hochstetter and 🆔 Elke Neu

View Online **Export Citation** **CrossMark**

ARTICLES YOU MAY BE INTERESTED IN
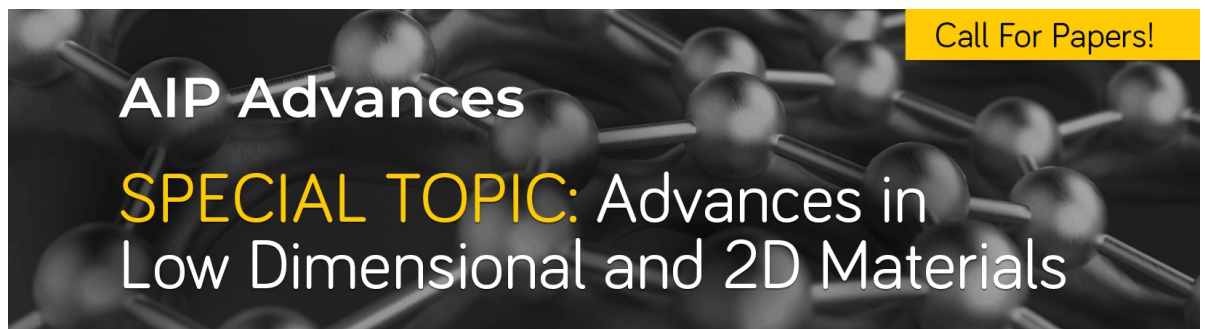
Quantum computer based on color centers in diamond
Applied Physics Reviews **8**, 011308 (2021); https://doi.org/10.1063/5.0007444

Direct writing of high-density nitrogen-vacancy centers inside diamond by femtosecond laser irradiation
Applied Physics Letters **118**, 214001 (2021); https://doi.org/10.1063/5.0049953

A flexible nitrogen-vacancy center probe for scanning magnetometry
Review of Scientific Instruments **92**, 055001 (2021); https://doi.org/10.1063/5.0040679

Call For Papers!

AIP Advances

SPECIAL TOPIC: Advances in Low Dimensional and 2D Materials

11, 065006

Multi-color laser excitation of diamond nitrogen vacancy centers embedded in nanophotonic structures

View Online   Export Citation   CrossMark

Axel Hochstetter [ID] and Elke Neu[a) [ID]

AFFILIATIONS

Department of Physics, TU Kaiserslautern, Erwin Schrödinger Straße, Building 56, 67663 Kaiserslautern, Germany

[a)]Author to whom correspondence should be addressed: nruffing@rhrk.uni-kl.de

ABSTRACT

Negatively charged nitrogen vacancy centers (NV⁻) in diamond serve as highly sensitive, optically readable sensors for magnetic fields. Improved sensing approaches rely on NV⁻ centers embedded in diamond nanopillar waveguides, which enable scanning probe imaging and use multi-color laser schemes for efficient spin readout. In this work, we investigate the free-beam coupling of the most relevant laser wavelengths to diamond nanopillars with different geometries. We focus on cylindrical pillars, conical pillars, and conical pillars with an added parabolic dome. We study the effects of the pillar geometry, NV⁻ position, laser wavelength, position of laser focus, and excitation geometry (excitation from the top facet or from the substrate side). We find a pronounced impact of the laser wavelength that should be considered in multi-color excitation of NV⁻. Within the pillars, exciting laser fields can be enhanced up to a factor of 11.12 compared to bulk. When focusing the laser to the interface between the substrate and the nanopillar, even up to 29.78-fold enhancement is possible. Our results are in accordance with the experimental findings for green laser excitation of NV⁻ in different pillar geometries.

I. INTRODUCTION

Optically active point defects in diamond, termed color centers, are atom-like quantum systems. They are applied in various fields ranging from life science, where they serve as non-bleaching fluorescent labels,[1] to quantum technologies, where their use spans from quantum sensing (e.g., Ref. 2) to quantum communication and computing.[3] For all these applications, efficiently collecting and detecting the color center's photoluminescence (PL) is a central challenge. Especially in quantum technologies, emitted PL photons serve two purposes: on one hand, color centers serve as a single photon source, where the emitted photons will encode information, e.g., in quantum cryptography or photons mediate interactions between distant color centers (spin–photon and spin–spin entanglement[3]). On the other hand, for some color centers, the PL's brightness is directly linked to the color center's electronic spin state [spin-dependent PL, optically detected magnetic resonance (ODMR[4])]. The latter is especially prominent for negatively charged nitrogen vacancy (NV⁻) centers in diamond: ODMR enables using even

individual NV⁻ centers, e.g., as highly sensitive magnetic sensors under ambient conditions.[5] For this purpose, typically green laser light (532, 510 nm) excites NV centers non-resonantly. However, due to diamond's high refractive index (n = 2.4 for visible light), only a few percent of NV⁻ PL are typically collected from bulk diamond.[6] Consequently, in the last ten years, waveguide-like nanostructures have been developed and employed to efficiently collect the ~100 nm broad PL band of NV⁻ and to facilitate non-resonant spin readout.[7–13] In parallel, improved optical spin readout schemes for NV⁻ emerged that do not directly rely on ODMR: in 2012 and 2013, three publications reported that yellow laser light (typically ~594 nm) selectively excites NV⁻, while for time intervals at which the same center is ionized to NV⁰ no excitation and consequently no PL occurs. This enables us to read out the NV charge state with high fidelity.[14–16] Non-resonant NV⁻ spin readout relies on a spin-dependent inter-system crossing to long-lived singlet states. Additionally, residing in the singlet states protects NV⁻ efficiently from being ionized to NV⁰ under resonant excitation of the triplet transitions. Consequently, via this spin-state dependent ionization

probability, the NV⁻ spin state is converted into a charge state when adding (close-to) resonant excitation with red laser light addressing the purely electronic transition (ZPL) at 637 nm.[17] In summary, highly efficient, optical NV⁻ spin readout nowadays relies on three-color pulse sequences with red, yellow, and green laser light (see, e.g., Ref. [18]). While the effect of diamond waveguides, especially tip-like, close-to cylindrical nanopillars (NPs), on the NV⁻ PL has been extensively researched,[7–12] the effect of NPs on the laser light used to manipulate NV⁻ has not been investigated. In this article, we present extensive numerical simulations to reveal how well typical Gaussian laser beams couple into NPs. As diamond NPs often serve as scanning probes, they are manufactured on thin diamond membranes (<1 μm) to ease mounting in a scanning probe microscope.[19] This allows for two excitation geometries: from the NP top facet and from the membrane side. We include these two options in our simulations. We investigate the influence of the NP geometry and laser wavelength and compare our results to the experimental findings.

II. SIMULATION SETUP

We performed all computations using commercially available finite difference time domain (FDTD) software (Lumerical FDTD-solutions, Version 2020 R6 on CentOS7). The excitation lasers were simulated using a Gaussian laser source of parallel linearly polarized light with a size (as defined by the power dropping to $1/e^2$) of 2 by 2 μm. The source was positioned at the origin (0/0/0), with the light propagating along the negative z axis. The light intensity (x–y plane) and the source's spectrum (wavelengths set to range from 500 to 900 nm) resembled a Gaussian fundamental mode (see Fig. 2). The electric field vector oscillated along the x axis and orthogonal to the magnetic field (y axis). The intensities were set to an amplitude of 1 to facilitate standardization.

For the upright setup (shown in Fig. 1), we positioned the source 0.5 μm above the NP's surface (the results are shown in Fig. 3).

For the inverted setup, the source remained at the same position, while the structure would be inverted: the diamond membrane (purple in Fig. 1) would be topmost, with the NPs (yellow in Fig. 1) pointing downward. In the inverted setup, we investigated two laser foci: (a) 10 nm below the surface of the diamond membrane (the results are shown in Fig. 4) and (b) at the interface between the diamond membrane and the NP (the results are shown in Fig. 5). We chose to investigate two focus options due to the following reasons: experimentally, focusing is optimized by maximizing the detected PL count rates. However, when exciting color centers below saturation, enhanced PL rates reflect a combination of enhanced PL collection efficiency and enhanced excitation intensity for different objective positions. We thus investigate two different potentially optimal foci to get a more complete picture.

We enabled the software's options to eliminate discontinuities and to optimize for short pulse. We activated the option to let the beam fill a thin lens with an NA of 0.8 and set the focus to be in the layer of the simulated NVs, 10 nm below the top surface of the NP. We chose a depth of 10 nm for the NV layer; as such shallow NVs are very typical for sensing applications. The above described option, which is offered by Lumerical, allowed us to calculate the effects of a focusing lens without having to explicitly model the lens and the
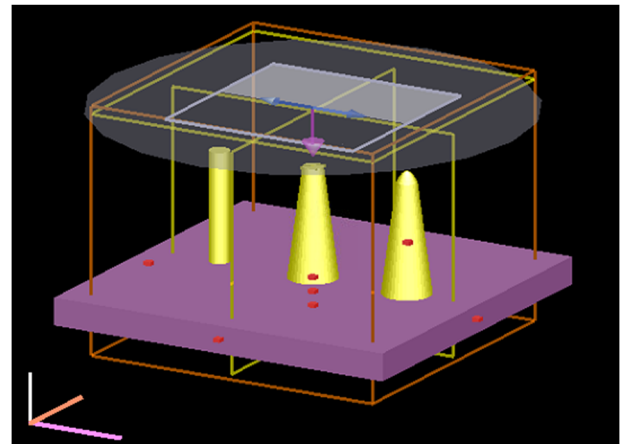

FIG. 1. Representation of the simulation setup. We place diamond nanopillars (NPs, yellow) on a diamond membrane (purple, 500 nm thick). We assume NV centers to be placed 10 nm below the top facet of the NPs for cylinder (left) and truncated cone (middle). As the third geometry, we add recently investigated NPs that resemble a truncated cone with a parabolic dome on top (right).[12] We assume that in the domed cone, NVs will be placed in the same height as in the other NPs. The parabolic dome is simply added on top. While the light has to travel further in this NP, its geometry should aid focusing it toward the center of the NV layer. Thus, also for the dome-shaped NP, monitors are flat and record light intensity in the xy plane. All cones have a slope of 4°, which is in agreement with the experimental findings,[6,12] and a height of 2 μm. The top facet has a radius of 0.1 μm, and the bottom radius of the NP is 0.1 μm for the cylinder and 0.24 μm for the cone and the domed cone. The dome itself has a radius of 0.1 μm in x and a height of 0.2 μm in z. The laser light is represented by a Gaussian mode (gray), coming from top, being coupled into the NPs, and out through the membrane. Scale bars are 1 μm.

light traveling all the distance. We thus modeled the very common experimental situation in which a parallel laser beam is focused onto the NP using an air objective,[8,19] while minimizing the simulation volume. The beam was constructed by adding up a total of 400 plane waves.

The entire simulation volume was sectioned using a uniform mesh with a mesh size of 5 nm for all three Cartesian coordinates. Figure 1 depicts the simulation setup. Note that in Fig. 1, we depict all three NP geometries simultaneously, while the simulations have been run for only one NP geometry at a time.

To record the results, our setup included three 2D monitors spanning the xy plane: one at the position where NV centers would be placed (here, 10 nm below the NP's top surface), below the membrane, and above the source. Using the monitor at the NV level, we gathered data about the light intensity reaching the NV centers (see Fig. 2). The monitor below the membrane on the other hand was added to record the amount of light traversing the entire diamond structure, while the monitor above the source recorded data on the light reflected by the diamond structure. The data to record were set to "standard Fourier transform," total spectral average, and all Poynting vectors (Px, Py, Pz) and output power (P). This ensured that the Poynting vectors were all normalized and directly comparable to each other for various simulations.

To calculate and normalize the excitation laser light intensity available at the presumed NV location, we used the real part $\mathfrak{R}$ of the magnitude of the Poynting vector ($|S|$, unit W/cm²). The Lumerical
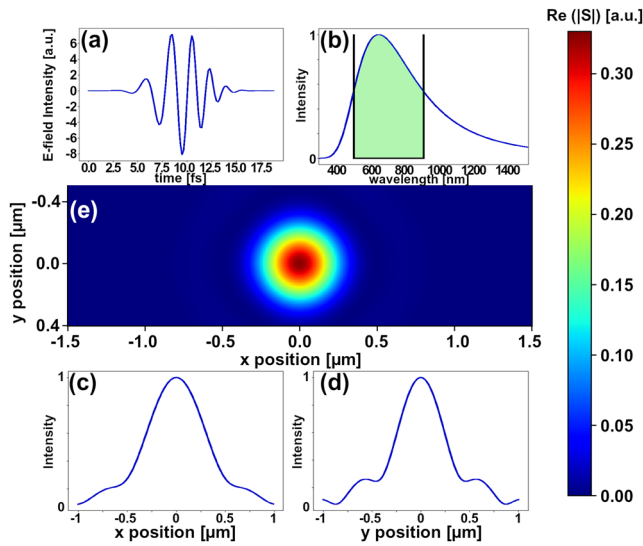
FIG. 2. Characterization of the laser source and the resulting Poynting vector in diamond that serves as a reference. (a) Intensity profile of the pulse emitted at the laser source (intensity vs time). (b) Spectrum of the radiation emitted by the laser source (intensity vs wavelength). The green area (500–900 nm) represents the spectrum set in Lumerical to be calculated. (c) and (d) Intensity profiles of the electric field of the emitted radiation at the source: along the x axis (c) and the y axis (d). (e) False-color representation of the real part of the resulting Poynting vector across the NV layer—10 nm below the surface of bulk diamond—for a wavelength of 532 nm. This was used as a reference for all enhancement factor calculations of 532 nm.

software employs Parseval's theorem to link the power P flowing through a surface A (i.e., the plane we monitor) to which the Poynting vector S is orthogonal $_\perp$. For a plane wave, this relation can be described as

$$P = \int \Re S_\perp \, dA = \sum_{x,y=0}^{j,k} \Re S_\perp (x,y). \qquad (1)$$

While the usage of plane waves is an approximation, we ran a series of pre-calculations and found that already using 40 plane waves, the addition of further plane waves did not significantly change the results. To further increase the accuracy, we used a total of 400 plane waves and summed up to model the Gaussian laser source. For microscopic models as ours, the Poynting vector can be derived from the differential Maxwell equations and can be expressed as the following cross product ($\times$):

$$S = \frac{1}{\mu_0} E \times B, \qquad (2)$$

where μ_0 is the vacuum permeability, E is the electric field vector, and B is the magnetic field vector. Since the Poynting vector is defined to be always orthogonal to both the electric and magnetic field vectors [see Equation (2)], we limit our calculations to the part of the Poynting vector that is orthogonal to the electrical and magnetic field vectors, $S_\perp$.

To ensure that the obtained Poynting vectors are comparable across all our simulations, it proved vital to use the same settings (see above) for all monitors.

The magnitude of the Poynting vector was recorded for the entire mesh-layer using the 2D monitor placed 10 nm below the NP's facet and thus at the presumed NV position.

For reference, we simulated the situation where NV centers are incorporated into bulk diamond by using a 2D monitor parallel to the diamond surface and 10 nm below the surface of bulk diamond. We employ the same Gaussian source as for the NP geometry. The sum of the power flowing through this layer, P_{xy}^0, was calculated by

$$P_{xy}^0 = \sum_{x,y=0}^{j,k} \Re S_\perp (x,y)^0. \qquad (3)$$

Here, the summation over $\sum_{x,y=0}^{j,k}$ denotes the summation over all mesh points in the monitor plane. $\Re S_\perp$ again denotes the real part of the Poynting vector that is orthogonal to the plane through which it flows. The superscript ^{0} marks the values in bulk (as reference). Simulations of other geometries are annotated by ^{g} instead of ^{0}. Here, geometry includes the geometry of the pillar (cylinder, truncated cone, and domed cone) and of the setup (upright or inverted excitation). For explanation, see Fig. 1. All values refer to a z-coordinate 10 nm below the surface of the cylinder, bulk, membrane, or truncated cone, and 10 nm below the domed cone section, to keep the simulations inter-comparable. We note that this leads to a strongly increased distance to the apex for the domed cone geometry but places the NVs in NP areas with similar cross sections for all geometries, thus rendering simulation results
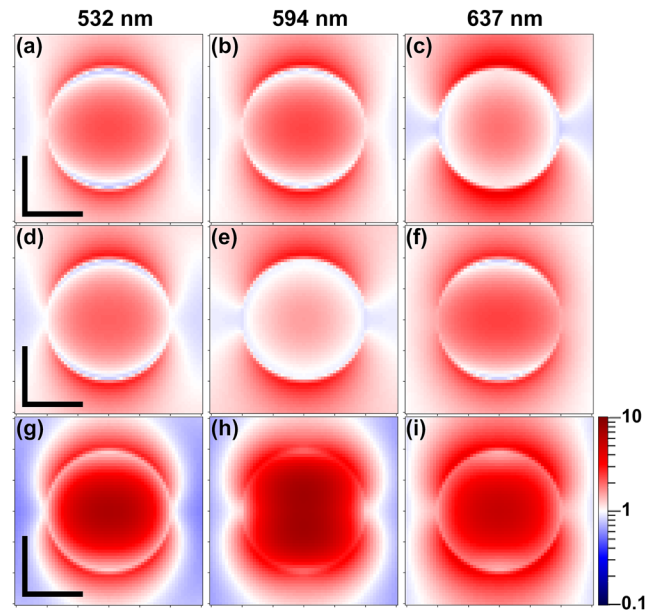

FIG. 3. Simulation results for upright setups. The graph displays a color coded map of the enhancement factor $\varepsilon_{xy}(\lambda)$ on a logarithmic scale, 10 nm below the NP facet (the plane in which we assume the NV center to be placed). The different panels show the results for NPs shaped like a cylinder [top row, (a)–(c)], truncated cone [middle row, (d)–(f)], and domed cone [bottom row, (g)–(i)] and at the important NV wavelengths of $\lambda_{laser} = 532$ nm [left column, (a), (d), and (g)], $\lambda_{laser} = 594$ nm [center column, (b), (e), and (h)], and $\lambda_{laser} = 637$ nm [right column, (c), (f), and (i)], respectively. The scale bar is 100 nm.
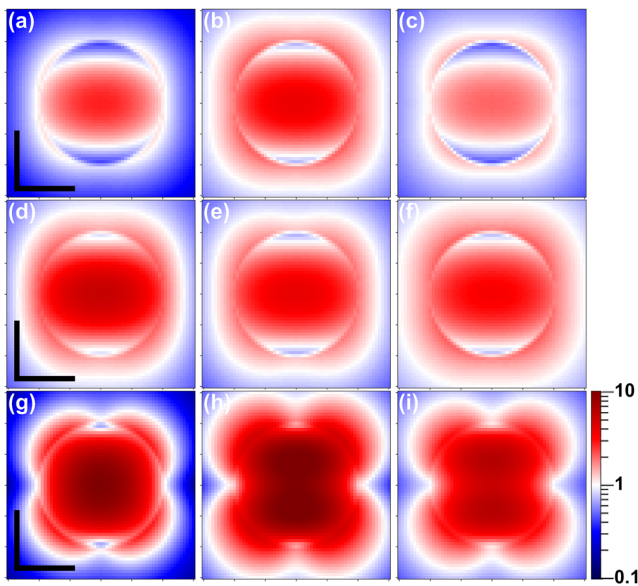
FIG. 4. Simulation results for the inverted setups. The false-color scale is the same for all images, going from dark blue (0.1) to dark red (10) with white denoting the center at 1. The different panels show the results for different pillars: (a)–(c) cylinder, (d)–(f) cone, and (g)–(i) domed cone. The scale bar is 100 nm.

more comparable. The magnitude of the Poynting vector reference P_{xy}^0 and the geometry and spectrum of the simulated laser source, which is typical for a confocal microscope, are shown in Fig. 2.
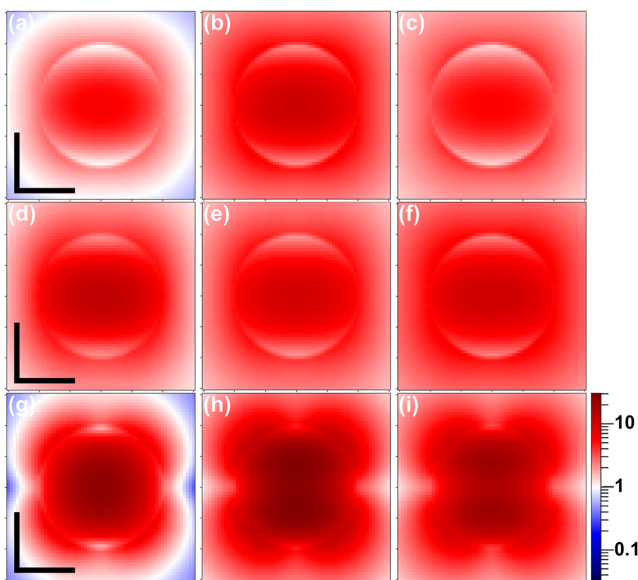

FIG. 5. Simulation results for inverted setups, where the laser was focused to the interface between membrane and waveguide. The false-color scale is the same for all images, going logarithmically from dark blue (1/30) to dark red (30) with white denoting the center at 1. The different panels show the results for different pillars: (a)–(c) cylinder, (d)–(f) cone, and (g)–(i) domed cone. The scale bar is 100 nm.

To calculate how any NP geometry influences the laser light intensity reaching the NV layer, we employed Eq. (4). For each geometry and wavelength, the values of the Poynting vector magnitude at each position of the mesh $P_{xy}^g(\lambda)$ were subsequently compared to the corresponding values obtained from the bulk diamond simulation $P_{xy}^0(\lambda)$. This point-by-point division leads to the enhancement factor ε of the geometry g at these coordinates xy for the selected wavelength (λ); see the following equation:

$$\varepsilon_{xy}^g(\lambda) = \frac{P_{xy}^g(\lambda)}{P_{xy}^0(\lambda)}. \tag{4}$$

The results were converted from matrices into pictures (Figs. 3–5) and exported using self-written Python scripts.

III. RESULTS AND DISCUSSION

As to be expected from our simulation setup, we can identify an axial dependency of the electromagnetic fields in all our setups (see Figs. 3 and 4), caused by the linear polarization of the laser source. This is most pronounced in the evanescent fields traveling outside the NP waveguide in Fig. 3 that exhibit a crescent shape with the x axis as the long axis, and the y axis as the short axis. Inside the NP, the enhancement ε exhibits mostly elliptical shapes—also with the x axis as the long axis. The strength and exact shape of the enhancement ε, however, significantly depend on the laser wavelength λ_{Laser} as well as the NP's geometry. For the cylindrical and domed cone geometry, the evanescent fields that propagate into the side surface of the waveguides can cause a high local enhancement for any NV center located at these fringes. However, since the evanescent fields experience an exponential dampening when penetrating into the waveguide, we excluded these high enhancements factors in Table I due to their extreme gradients.

As can be seen in Fig. 4, in the inverted setup, the evanescent fields are dampened compared to the standard setup (see Fig. 3). Inside the NP, the field intensity depends not only on the setup (upright or inverted), but also on the geometry of the NP and the wavelength of the laser (see Table I). While cylindrical and coni-

TABLE I. Maximal enhancement factors ε within the NP, 10 nm below the NP facet, listed by wavelength and geometry.

Waveguide geometry (nm)	532 (nm)	594 (nm)	637 (nm)
Cylinder	2.23	2.30	1.89
Truncated cone	2.03	1.54	2.36
Dome	6.55	7.27	5.25
Inverted cylinder	2.74	3.73	2.01
Inverted truncated cone	5.27	3.82	3.34
Inverted dome	9.91	11.12	6.14
Inverted cylinder, focused on the NP interface	6.23	11.23	5.83
Inverted cone, focused on the NP interface	13.51	10.24	10.82
Inverted dome, focused on the NP interface	25.23	29.78	20.25

cal NPs always have the strongest enhancement in the center, this holds not true for the domed cone geometry. From the simulations recorded, it is clear that reflection occurring on the perpendicular membrane's surface has some impact, but is not the only driving force for evanescent fields. Due to the geometry of the NPs, these evanescent fields also exist within the photonic modes of the NPs themselves, as discussed in detail by Fuchs *et al.* in 2018.[6] The highest enhancement factors ε can be achieved using domed cones as waveguides (see Table I). This holds true for all investigated wavelengths, and no matter whether the light is coupled directly into the waveguide in the upright setup or has to cross the membrane in the inverted setup. Throughout all wavelengths and geometries, the inverted setup exhibits consistently higher enhancement factors ε. These findings are very promising for scanning probe-based sensing approaches as the inverted geometry is often used in these approaches. Moreover, dome cones have also been found to be an optimal geometry considering the enhancement of the collection of NV fluorescence.

In addition, we repeated the simulations of the inverted setup, where the laser was focused 500 nm deeper into the diamond. The focus thus changed from 10 nm below the membrane's surface to the interface between the membrane and the NP waveguide. The results (see Fig. 5) show that this increases the enhancement factor even further, by another factor of roughly 2.5 for any combination of geometry and wavelength.

The different intensities at different wavelengths can be explained by the Fabry–Pérot interference along the NPs. To that end, we plotted an overview of the relative intensities of the light reaching the NV layer in different geometries vs their wavelengths in Fig. 6.
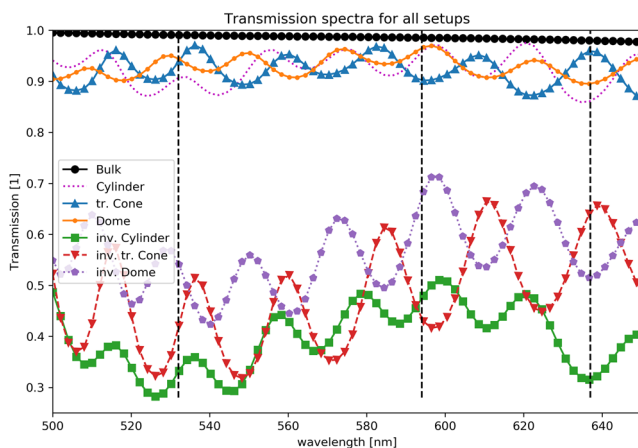

FIG. 6. Simulation results for all setups. Depicting how much of the light for each wavelength gets transmitted to the layer of the NV. The oscillations are the results of the Fabry–Pérot interference along the NPs. All graphs are not normalized but grouped for comparison. Black solid circles represent the infinite bulk of diamond. Fine magenta dots represent the cylindrical wave guides. Closed blue upward triangles represent the truncated cones, and orange circles represent domed cones. The inverted setups are represented by green closed squares (cylinders), red downward pointing triangles (truncated cones), and lilac closed pentagons (domed cones), respectively. Vertical black dashed lines show the wavelengths of 532, 594, and 637 nm.

IV. CONCLUSION AND OUTLOOK

The simulations presented within this article clearly demonstrate the pronounced impact of the geometry of the NP waveguides on the relative availability of light within the NP waveguides. They also show the clear advantage of the domed cone geometry over the truncated cone and the cylindrical geometry. With the domed cone geometry, it is possible to increase the excitation laser intensity available to NVs placed at any point along the studied plane by a factor of 5–11, depending on the wavelength and setup orientation. The better enhancement of domed cones vs truncated cones can be explained by the refraction of light entering the dome: along the hyperbolic curvature of the dome, all light is refracted toward the focal point inside the dome. This drastically increases the amount of light directed to the plane of the NVs. Videos of these simulations are available at https://doi.org/10.5281/zenodo.4727903. This increase is in good agreement with experimental data for 532 nm laser excitation stating that in photonic structures comparable to our NPs, NV centers can be efficiently excited showing saturation powers of down to 100 μW together with a strong enhancement in fluorescence collection. Consequently, the NPs increase the signal to background ratio compared to bulk diamond[9] and enable more efficient sensing. In 2020, McClosekey *et al.* studied similar arrays of domed cone structures [see Fig. 1(b) in Ref. 11]. For a fixed low excitation power (55 μW), the NV photoluminescence is enhanced by a factor of 11.5. While both these experimental results are first hints that the fluorescence collection and excitation laser intensity are both enhanced in the NPs, the random placement of the NV centers as well as a potential spread of absorption cross sections of the NV centers hinders reliable determination of the laser intensity available to the NV centers. Our calculations provide information on the distribution of laser intensity in the NP.

We find a higher light availability toward the center of the NP waveguide and a potential for less light availability toward the rim of the wave guides. The domed cones exhibit the best enhancement, and the inverted setup further increases the amount of light reaching the NVs.

Our simulations provide important guidance for experiments using multiple excitation lasers applied to the NV centers: enhancement factors for the three most common wavelengths in multi-color experiments differ strongly: for example, for the inverted setup with the domed cone NP, the enhancements for 594 and 637 nm lasers differ by almost a factor of two (11.1/6.1). In contrast, for the inverted setup with the truncated cone NP, the enhancement for those wavelengths differs only by 10% (3.8/3.4). Consequently, optimal laser powers or laser power ratios of the lasers in bulk experiments might differ from those in NPs and will also change with the NP geometry. Our simulation data aid in adjusting laser powers used for optimized multi-color sensing experiments in different NP geometries.

DATA AVAILABILITY

The data that support the findings of this study are available from the corresponding author upon reasonable request.

REFERENCES

[1] M. Chipaux, K. J. van der Laan, S. R. Hemelaar, M. Hasani, T. Zheng, and R. Schirhagl, "Nanodiamonds and their applications in cells," Small **14**, 1704263 (2018).

[2] F. Casola, T. van der Sar, and A. Yacoby, "Probing condensed matter physics with magnetometry based on nitrogen-vacancy centres in diamond," Nat. Rev. Mater. **3**, 17088 (2018).

[3] B. Hensen, H. Bernien, A. E. Dréau, A. Reiserer, N. Kalb, M. S. Blok, J. Ruitenberg, R. F. L. Vermeulen, R. N. Schouten, C. Abellán et al., "Loophole-free bell inequality violation using electron spins separated by 1.3 kilometres," Nature **526**, 682–686 (2015).

[4] A. Gruber, A. Dräbenstedt, C. Tietz, L. Fleury, J. Wrachtrup, and C. von Borczyskowski, "Scanning confocal optical microscopy and magnetic resonance on single defect centers," Science **276**, 2012 (1997).

[5] M. Radtke, E. Bernardi, A. Slablab, R. Nelz, and E. Neu, "Nanoscale sensing based on nitrogen vacancy centers in single crystal diamond and nanodiamonds: Achievements and challenges," Nano Futures **3**, 042004 (2019).

[6] P. Fuchs, M. Challier, and E. Neu, "Optimized single-crystal diamond scanning probes for high sensitivity magnetometry," New J. Phys. **20**, 125001 (2018).

[7] T. M. Babinec, B. J. M. Hausmann, M. Khan, Y. Zhang, J. R. Maze, P. R. Hemmer, and M. Lončar, "A diamond nanowire single-photon source," Nat. Nanotechnol. **5**, 195–199 (2010).

[8] P. Maletinsky, S. Hong, M. S. Grinolds, B. Hausmann, M. D. Lukin, R. L. Walsworth, M. Loncar, and A. Yacoby, "A robust scanning diamond sensor for nanoscale imaging with single nitrogen-vacancy centres," Nat. Nanotechnol. **7**, 320–324 (2012).

[9] E. Neu, P. Appel, M. Ganzhorn, J. Miguel-Sánchez, M. Lesik, V. Mille, V. Jacques, A. Tallaire, J. Achard, and P. Maletinsky, "Photonic nano-structures on (111)-oriented diamond," Appl. Phys. Lett. **104**, 153108 (2014).

[10] S. A. Momenzadeh, R. J. Stöhr, F. F. de Oliveira, A. Brunner, A. Denisenko, S. Yang, F. Reinhard, and J. Wrachtrup, "Nanoengineered diamond waveguide as a robust bright platform for nanomagnetometry using shallow nitrogen vacancy centers," Nano Lett. **15**, 165–169 (2015).

[11] D. J. McCloskey, N. Dontschuk, D. A. Broadway, A. Nadarajah, A. Stacey, J.-P. Tetienne, L. C. L. Hollenberg, S. Prawer, and D. A. Simpson, "Enhanced widefield quantum sensing with nitrogen-vacancy ensembles using diamond nanopillar arrays," ACS Appl. Mater. Interfaces **12**, 13421–13427 (2020).

[12] N. Hedrich, D. Rohner, M. Batzer, P. Maletinsky, and B. J. Shields, "Parabolic diamond scanning probes for single spin magnetic field imaging," Phys. Rev. Applied **14**, 064007 (2020); arXiv:2003.01733.

[13] S.-W. Jeon, J. Lee, H. Jung, S.-W. Han, Y.-W. Cho, Y.-S. Kim, H.-T. Lim, Y. Kim, M. Niethammer, W. C. Lim et al., "Bright nitrogen-vacancy centers in diamond inverted nanocones," ACS Photonics **7**, 2739 (2020).

[14] K. Beha, A. Batalov, N. B. Manson, R. Bratschitsch, and A. Leitenstorfer, "Optimum photoluminescence excitation and recharging cycle of single nitrogen-vacancy centers in ultrapure diamond," Phys. Rev. Lett. **109**, 097404 (2012).

[15] P. Siyushev, H. Pinto, M. Vörös, A. Gali, F. Jelezko, and J. Wrachtrup, "Optically controlled switching of the charge state of a single nitrogen-vacancy center in diamond at cryogenic temperatures," Phys. Rev. Lett. **110**, 167402 (2013).

[16] N. Aslam, G. Waldherr, P. Neumann, F. Jelezko, and J. Wrachtrup, "Photo-induced ionization dynamics of the nitrogen vacancy defect in diamond investigated by single-shot charge state detection," New J. Phys. **15**, 013064 (2013).

[17] B. J. Shields, Q. P. Unterreithmeier, N. P. de Leon, H. Park, and M. D. Lukin, "Efficient readout of a single spin state in diamond via spin-to-charge conversion," Phys. Rev. Lett. **114**, 136402 (2015).

[18] A. Ariyaratne, D. Bluvstein, B. A. Myers, and A. C. B. Jayich, "Nanoscale electrical conductivity imaging using a nitrogen-vacancy center in diamond," Nat. Commun. **9**, 2406 (2018).

[19] P. Appel, E. Neu, M. Ganzhorn, A. Barfuss, M. Batzer, M. Gratz, A. Tschöpe, and P. Maletinsky, "Fabrication of all diamond scanning probes for nanoscale magnetometry," Rev. Sci. Instrum. **87**, 063703 (2016).